How to cite: *Angew. Chem. Int. Ed.* **2023,** *62,* e202303616
doi.org/10.1002/anie.202303616

Li-Ion Batteries | Hot Paper

# Braided Fiber Current Collectors for High-Energy-Density Fiber Lithium-Ion Batteries

*Xinlin Huang[+], Chuang Wang[+], Chuanfa Li, Meng Liao, Jiaxin Li, Haibo Jiang, Yao Long, Xiangran Cheng, Kun Zhang, Pengzhou Li, Bingjie Wang,* and Huisheng Peng**

**Abstract:** Fiber lithium-ion batteries represent a promising power strategy for the rising wearable electronics. However, most fiber current collectors are solid with vastly increased weights of inactive materials and sluggish charge transport, thus resulting in low energy densities which have hindered the development of fiber lithium-ion batteries in the past decade. Here, a braided fiber current collector with multiple channels was prepared by multi-axial winding method to not only increase the mass fraction of active materials, but also to promote ion transport along fiber electrodes. In comparison to typical solid copper wires, the braided fiber current collector hosted 139 % graphite with only 1/3 mass. The fiber graphite anode with braided current collector delivered high specific capacity of 170 mAh g$^{-1}$ based on the overall electrode weight, which was 2 times higher than that of its counterpart solid copper wire. The resulting fiber battery showed high energy density of 62 Wh kg$^{-1}$.

Flexible and lightweight fiber lithium-ion batteries (FLIBs) that well meet the requirements of portable and wearable electronics have recently spurred extensive research interests.[1] Thus far, most efforts have been devoted to improving electrochemical performances of FLIBs by developing high-capacity materials,[2] but the energy densities of FLIBs based on the overall devices are still insufficient for practical applications.[3] Besides the development of active materials, it is also necessary to design novel architectures of fiber electrodes to load more active materials and promote charge transports for high energy densities of FLIBs.[4] Unfortunately, it remains unavailable for this direction, possibly because it has been long recognized that a fiber battery is generally produced by twisting a fiber anode and a fiber cathode, and there is very limited space on designing novel architectures for fiber electrodes.

Fiber electrodes had been widely prepared from a variety of carbon-based fibers as current collectors,[5] but they suffered from low electrical conductivities and limited electron transport efficiencies from active materials to current collectors.[6] In particular, due to low electrical conductivities of carbon-based fiber electrodes, the resulting FLIBs showed sharply decreasing electrochemical properties or even failed to work effectively with increasing lengths to meters required for real applications. The FLIBs from carbon-based fiber current collectors were thus limited to centimeters at laboratory level, and it is challenging to achieve continuous FLIBs.[7] To this end, they had also been made from metal materials like copper or aluminum wires as current collectors (Figure 1a).[8] They demonstrated high electrical conductivities and produced continuous FLIBs. However, they were solid and suffered from low surface areas for limited loading densities of active materials,[9] and the resulting thick active layers also showed poor ion transports to metal wires,[10] so the fabricated FLIBs demonstrated low energy densities.

Here a braided fiber current collector (BFCC) is prepared for FLIBs with high energy densities through a multi-axial winding method (Figure 1b, c). In our design, ultrathin metal wires were used as building blocks and woven into the BFCC, where ultrathin metal wires were aligned with each other to present high electrical conductivities on $10^7$ S m$^{-1}$ and form abundant channels that showed high loading content with linear density of 1.25 mg cm$^{-1}$, in comparison to 0.90 mg cm$^{-1}$ without braided structure. As a result, the use of BFCC achieved a triple mass-specific capacity and contributed to high energy density of 62 Wh kg$^{-1}$ based on the total weight of FILBs.

The BFCC could be continuously produced in tens of meters or even longer (Figure S1a) with high uniformity (Figure S1b), depending on the requirements of applications for FLIBs. Unlike the dense structure of solid fiber current collector (SFCC, Figure 1d, e), the building ultrathin metal wires in the BFCC moved forward in a helical pathway along the axial direction and were interwoven with each other to form aligned channels along the length direction (Figure 1f, g), which favored rapid and effective infiltrations of active material solutions/dispersions. Note that this multi-axial winding method can also be extended to other fiber current collectors, such as aluminum, stainless steel, nickel, and nylon wires (Figure S2). These braided fiber current

[*] X. Huang,[+] C. Wang,[+] Dr. C. Li, Dr. M. Liao, H. Jiang, Y. Long, X. Cheng, K. Zhang, P. Li, Prof. B. Wang, Prof. H. Peng
State Key Laboratory of Molecular Engineering of Polymers, Department of Macromolecular Science, and Laboratory of Advanced Materials, Fudan University
Shanghai 200438 (P. R. China)
E-mail: wangbingjie@fudan.edu.cn
penghs@fudan.edu.cn

J. Li
Department of Colloid Chemistry, Max Planck Institute of Colloids and Interfaces
Potsdam 14476 (Germany)

[+] These authors contributed equally to this work.

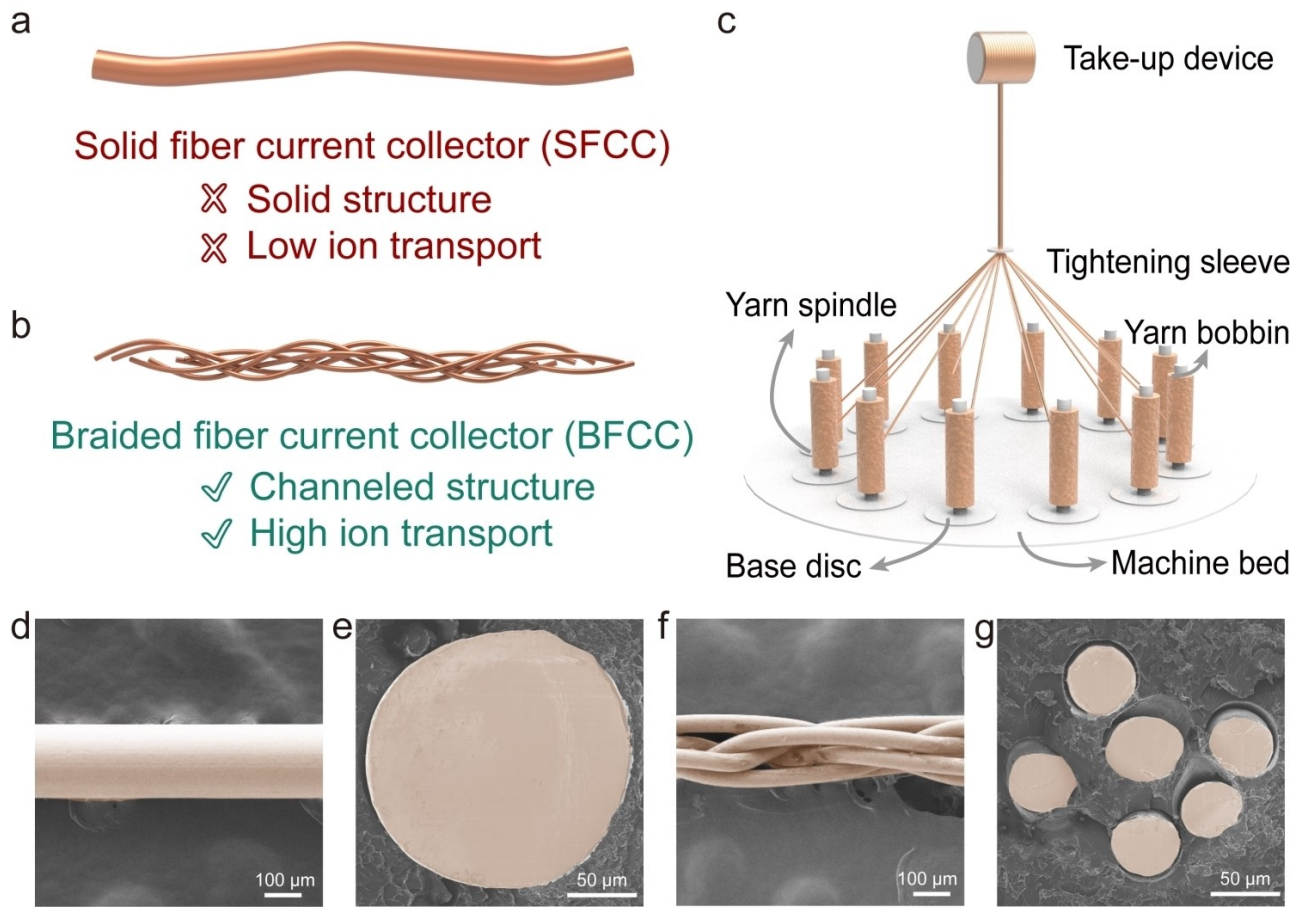


***Figure 1.*** Two types of fiber current collectors. a), b) Schematic of solid fiber current collector (SFCC) and braided fiber current collector (BFCC). c) Schematic illustration of preparing BFCC through a braiding process of multi-axial ultrathin metal wires. d), e) SEM images by top and side views of SFCC, respectively. f), g) SEM images by top and side views of BFCC, respectively.

collectors are also promising for other fiber electronic devices like supercapacitors, solar cells, and sensors. Here the number of channels could be controlled by braiding different numbers (e.g., 1 to 12) of ultrathin metal wires with different diameters (e.g., 30, 50, and 80 μm) (Figure S3). These braided fibers were denoted as BFCC-*x*-*y*, where *x* and *y* represented the diameter and number of ultrathin metal wires, respectively. It was found that the proportion of channels reached a maximum at braiding number of 6 (Figure 2a). The finer the ultrathin metal wires were, the higher proportion of channels could be produced. Therefore, BFCC-30-6 showed the highest proportion of 69 %, but it suffered from relatively low breaking force (Figure 2b). It was found that BFCC-50-6 demonstrated a close proportion of 64 % and much higher breaking force, so it was selected for fabricating FLIBs unless specified otherwise. The cross section of BFCC-50-6 was approximated as a standard circle and the diameter was about 200 μm. To clearly show the advantages of braiding structure with multiple channels, SFCC with a comparable diameter of 200 μm and breaking force of 6.71 N was chosen as the control sample.

To further demonstrate the structural advantage of BFCC over SFCC, two types of fiber current collectors were coated with graphite slurry to prepare fiber electrodes, named BFCC-graphite (BFCC-G) and SFCC-graphite (SFCC-G) electrodes, respectively (Figure S4). By adjusting the coating speed, we had prepared fiber electrodes with tunable graphite mass loadings in good uniformity (Figure S5). For the diameter of fiber electrodes under the same loading content, BFCC-G was thinner than the corresponding control sample, proving that the channels did accommodate active materials (Figure S6). On the electrode level, a higher mass fraction of active material was beneficial to offer a higher mass-energy density. BFCC-G showed a superior mass fraction according to the calculation results (Figure S7), which reflected the structure advantage of the designed channels.

The increase of active materials resulted in an increased transport curve of lithium ions in the graphite electrode, leading to the decay of electrochemical performance.[11] Due to the decreased utilization of active materials, the capacity could not increase linearly with the increasing mass loading of graphite (Figure S8). Therefore, it was necessary to pursue high-loading contents while ensuring high electrochemical performances simultaneously. To verify the structure boost of BFCC for storage of Li ions in fiber electrodes, the half-cells were tested with the counter electrode of Li metal foil in the voltage range of 0.005–1.0 V. The specific

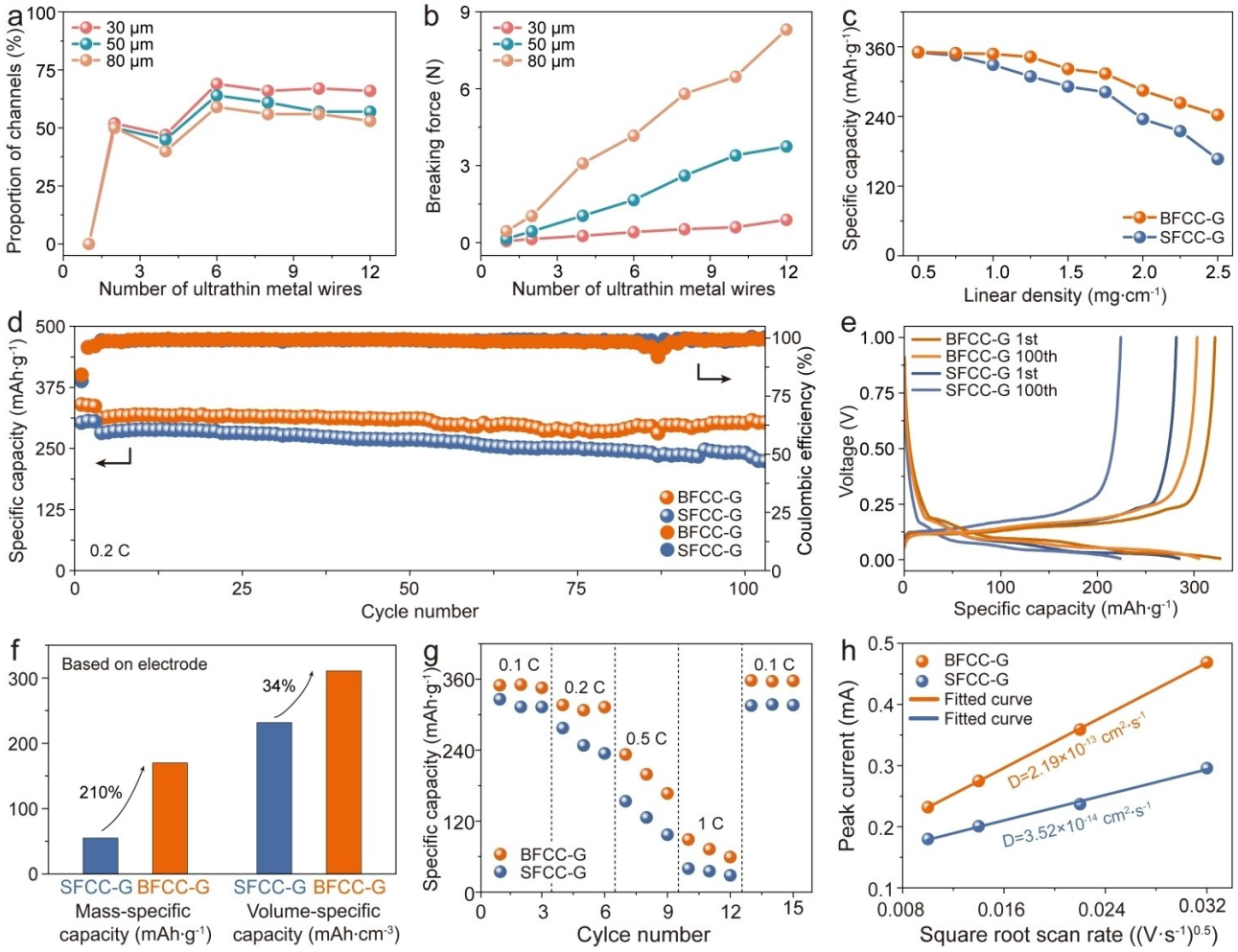


***Figure 2.*** Parameter optimization of BFCC and comparison on SFCC-G and BFCC-G electrodes. a), b) Effect of the braiding parameters on the (a) proportion of channels and (b) breaking forces of braided fibers. c) Dependence of specific capacity on linear density of graphite in two types of electrodes. d) Cycling performance at 0.2 C. e) Corresponding charge–discharge curves at 0.2 C at the 1st and 100th cycles. f) Comparison in mass/volume specific capacities based on the whole electrode. g) Rate performance. h) Plots of peak current versus square root scan rate of BFCC-G and SFCC-G based on their corresponding CV curves in Figure S14.

capacity of graphite on two kinds of fiber electrodes remained constant with increasing loading contents and then decayed successively (Figure 2c). Based on a normal specific capacity of graphite (340 mAh $g^{-1}$) as a standard, the BFCC-G electrode could achieve the highest loading content with linear density of 1.25 mg $cm^{-1}$, compared to 0.9 mg $cm^{-1}$ for the SFCC-G electrode under the same condition, indicating channels improved mass loadings of active materials (Figure S9). Therefore, all the following electrochemical performances were investigated at 1.25 mg $cm^{-1}$ to maximize the advantage of BFCC-G electrodes. To test the cycle stability against two electrodes, their cycle performances were compared at 0.1 C (Figure S10) and 0.2 C (Figure 2d). For stable growth of the solid electrolyte interface film, a charge/discharge rate of 0.1 C was set in the first three cycles at 0.2 C. The cycling tests showed outperformed reversible capacity of 312.4 mAh $g^{-1}$ for the BFCC-G electrode at 0.2 C along with enhanced capacity retention compared with that based on the SFCC-G electrode. The charge and discharge curves for the 100th cycle maintained the typical electrochemical characteristics of the graphite anode (Figure 2e).

Specific capacity was previously normalized only by the mass of active materials, ignoring the high dead weight of other inactive components. In this study, the specific capacity was calculated and normalized by the overall mass of the electrode, including active material, current collector, conductive additive, and binder. With the use of 0.2 C first-turn charging capacity as the basis for calculation, the mass-based and volume-based specific capacities of the BFCC-G electrode reached 170 mAh $g^{-1}$ and 310.75 mAh $cm^{-3}$, which showed 210 % and 34 % improvements than those of the SFCC-G electrode, respectively (Figure 2f). In addition, Al wires were also braided to demonstrate that the channel structure could also promote ion transport of lithium cobalt oxide (LCO) cathode electrode (Figure S11).

The facilitated transport kinetics induced from the BFCC-G electrode was further investigated through electrochemical measurements. The BFCC-G electrode exhibited

improved rate performance with capacities of 350.1 (0.1 C), 316.6 (0.2 C), 233 (0.5 C), and 89.2 mAh $g^{-1}$ (1 C) (Figure 2g). After charging at 1 C, the charge–discharge rate was reinstated to 0.1 C, and the charge capacity was maintained at 358.1 mAh $g^{-1}$. At various rates, it also had lower voltage gaps between the charge and discharge plateau (Figure S12).[12] This was also shown for electrodes with different mass loadings (Figure S13). According to CV curves measured at increasing scan rates from 0.1 to 1 mV $s^{-1}$ (Figure S14), the linear relationship between the peak current ($I_p$) and the square root of the scan rate ($v^{0.5}$) could be obtained, indicating a diffusion-controlled Faradaic process (Figure 2h).[13] The BFCC-G electrode showed a more significant slope of the $I_p$–$v^{0.5}$ curve, indicating a higher Li-ion diffusion coefficient ($D_{Li^+}$). Specifically, $D_{Li^+}$ of BFCC-G ($2.19\times10^{-13}$ $cm^2 s^{-1}$) derived from the Randles-Sevcik equation was superior to that achieved by SFCC-G ($3.52\times10^{-14}$ $cm^2 s^{-1}$). In the Nyquist plots, appropriate equivalent circuits were established to determine values of charge transfer resistance ($R_{ct}$) (Figure S15). BFCC-G showed a smaller $R_{ct}$ (49.3 Ω) than that of the control sample (74.4 Ω). Overall, the above results pointed to the significant enhancement of ion transport in the BFCC-G electrode with the design of channels.

To further understand the effect of channels on ion transport, cross-sectional scanning electron microscopy (SEM) images of fiber electrodes were collected (Figure 3a, b). For the SFCC-G electrode, graphite was uniformly covered on the surface of metal wire and formed a coaxial structure. In contrast, the graphite could be embedded in the channels and afforded seamless contact with the ultra-thin metal wires for the BFCC-G electrode. After the design of the corresponding two-dimensional cross-sectional model (Figure S16), the distribution of the electrode-level Li-ion concentration at the surfaces of graphite electrode particles was simulated using finite element simulation analysis at times of 60, 120, and 150 mins (Figure 3c). The initial concentration of Li ion in the graphite electrode was 10 mol $L^{-1}$. During discharge, the concentration in the graphite electrode increased as Li was dissolved from the Li

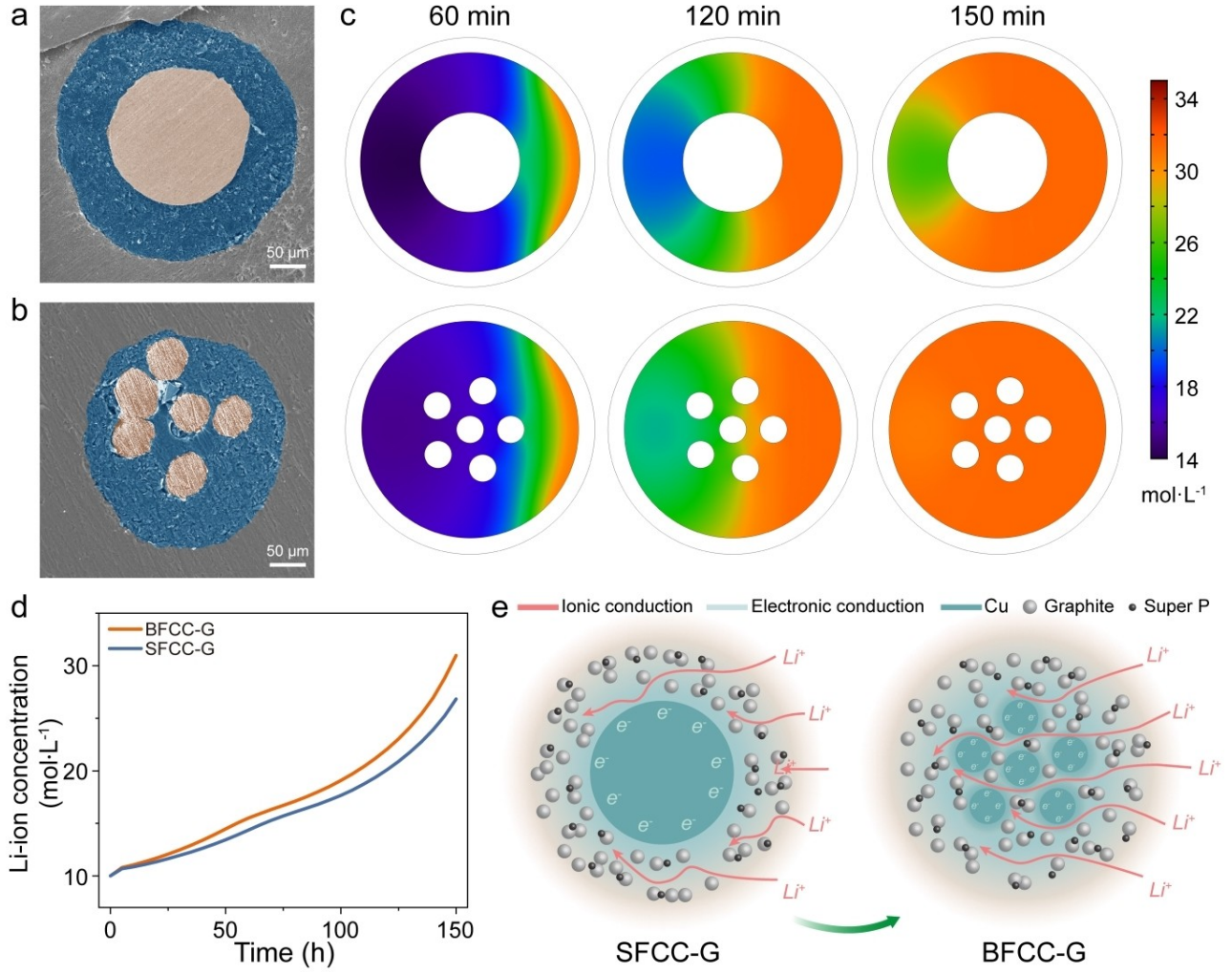


***Figure 3.*** Two-dimensional architecture visualization and simulation of ion transport in SFCC-G and BFCC-G electrodes. a), b) Cross-sectional SEM images of SFCC-G and BFCC-G with linear density of graphite as 0.5 mg $cm^{-1}$, respectively. c) Simulation of Li-ion concentration after discharging for 60, 120 and 150 mins. d) Dependence of Li-ion concentration on time. e) Schematic of Li-ion transfer pathways.

metal electrode. Li-ion accumulation on the side near Li and depletion on the side away from Li during cell operation induced large overpotentials in the electrode. It led to incomplete electroactive material utilization at the distal end while over-charging/discharging at the proximal end. For the BFCC-G electrode, ions can transport more rapidly from one end to the opposite, resulting in a lower concentration gradient of $Li^+$ in the electrode at different times. As the reaction proceeded, the concentration of the selected point on the BFCC-G electrode varied with time and gradually became higher than that on the SFCC-G electrode (Figure 3d), indicating that $Li^+$ reached the end away from the Li source more quickly in the former. As illustrated in Figure 3e, the channel structure of the BFCC may accommodate active materials to reduce $Li^+$ transport hindrance under the special coaxial relationship between the fiber current collector and the active layer. It facilitates $Li^+$ transport to the distal active material, improving capacity utilization and electrochemical performance.

To demonstrate the advantages of the BFCC-G electrode for high-energy-density FLIBs, the electrochemical performance of LCO-graphite full batteries was investigated using two different current collectors: LCO‖BFCC-G and LCO‖SFCC-G. The graphite loading with linear density of 1.25 mg cm$^{-1}$ had been used for both full batteries, and the positive LCO loading was adjusted so that the anode had 10% more total capacity than the cathode. The negative electrode was wrapped with a separator and twisted with the positive electrode (Figure 4a, b) to fabricate FLIBs of increasing lengths (Figure 4c). At each length, the LCO||BFCC-G batteries showed capacities approximately 10% higher than those of LCO||SFCC-G batteries (Figure 4d). The LCO||BFCC-G full battery also exhibited high cycling stability, with a capacity of 14.97 mAh and a coulombic efficiency of 99.75% after 100 charge–discharge cycles (Figure S17). In comparison, the capacity retention of the LCO||SFCC-G battery was only 12.5 mAh. Even at different current densities, LCO||BFCC-G batteries maintained high performances (Figure S18) due to their lower charge transfer resistances than those of LCO||SFCC-G batteries (Figure S19). In addition, the flexibility and durability of the LCO||BFCC-G FLIBs were investigated by repeated bending.[14] At a curvature radius of 5 mm, they showed a comparable 85.8% capacity retention to LCO‖SFCC-G FLIBs (83.0%) even after bending for 10,000 cycles (Figure S20). The energy density of the full battery, based on the total mass (including electrode, electrolyte, separator, and package), was calculated to reflect the actual specific energy of the battery. Compared with the conventional LCO||SFCC-G battery, the BFCC increased the energy density of FLIB by 18% from 52.09 to 61.67 Wh kg$^{-1}$ (see Figure S21 for the charge/discharge curves and Table S1 for the detailed parameters). The FLIBs were then woven to fabricate textile battery for

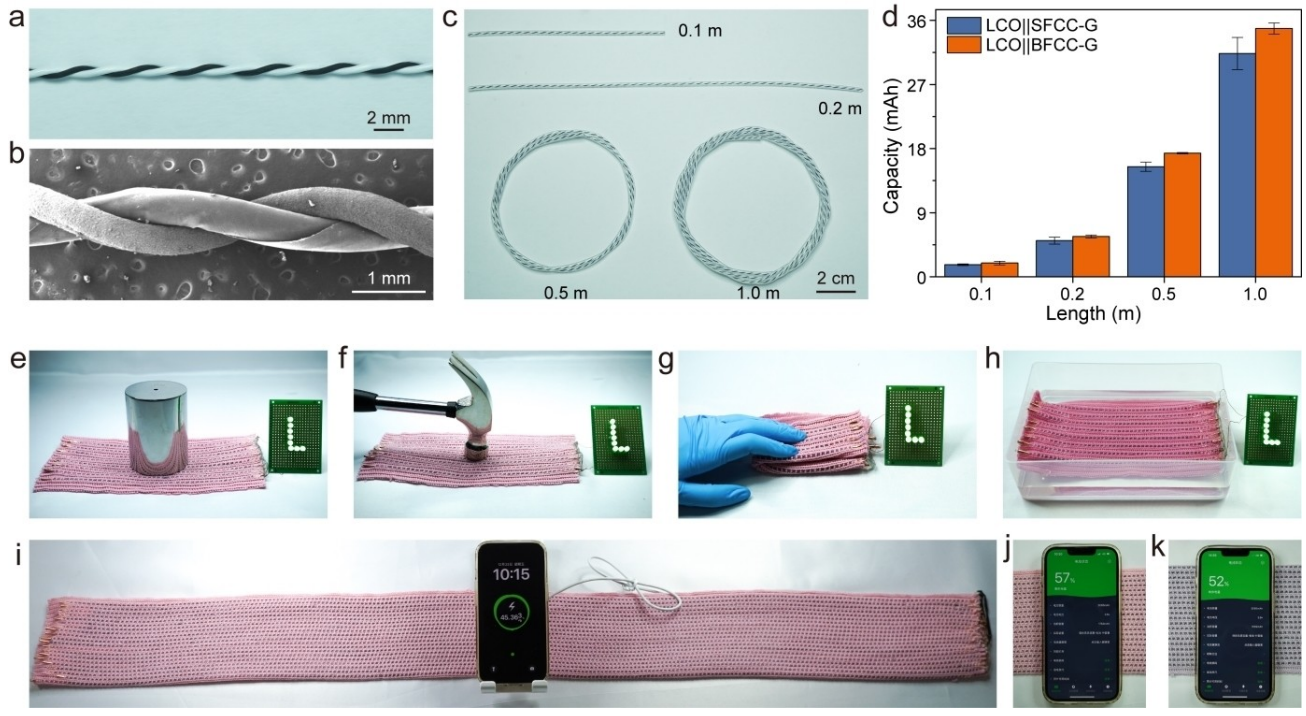


***Figure 4.*** Electrochemical performances and applications of FLIBs with LCO and graphite. a), b) Photograph and SEM image of a twisted FLIB, respectively. c) Photograph of FLIBs with increasing lengths. d) Capacity comparison at different lengths for SFCC-G and BFCC-G electrodes. e)–h) A textile battery consisting of FLIBs made from BFCC-G electrode to power light-emitting diodes stably under conditions of pressing, striking, folding and immersing in water, respectively. i) A textile battery woven by forty 1-m-long FLIBs made from BFCC-G electrode to charge a cell phone. j), k) Comparison of the charging capability for the cell phone by textile batteries woven with forty 1-m-long FLIBs made from SFCC-G and BFCC-G electrodes, respectively.

application demonstration. In detail, eight 0.2-m-long LCO||BFCC-G FLIBs were woven into a textile to power light-emitting device (Figure S22). The energy textile worked stably when pressed with 15 N, repeatedly hammered, folded, or immersed in water (Figures 4e–h). Even after wringing out the water from the soaked textile, the battery could stably power the light-emitting device (Figure S23). Further, forty 1-m-long LCO||BFCC-G FLIBs were successfully woven into a textile to charge a cell phone from 30 % to 57 % with about 30 mins, while the fabric woven with LCO||SFCC-G FLIBs could only charge the same cell phone to 52 % (Figures 4i–k and S24). Compared to conventional plate Li-ion batteries, the textile batteries exhibited flexibility, breathability, and weaveability, rendering them highly amenable for seamless integrations into fabrics intended for wearable applications.

In summary, we have designed a novel fiber current collector with both high electrical conductivity and loading content of active materials. The designed braiding structure leads to channels filled with active materials, reducing obstruction to $Li^+$ transport and increasing loading capability of active materials. As expected, the use of the BFCC has greatly improved the specific capacity and energy density of the FLIBs. This work offers a new and effective strategy to improve electrochemical performances of FLIBs by optimizing the architectures of fiber current collectors.

## Acknowledgements

This work was supported by STCSM (21511104900, 20JC1414902), NSFC (52222310, 22205039), and CPSF (2022M710733).

## Conflict of Interest

The authors declare no conflict of interest.

## Data Availability Statement

The data that support the findings of this study are available from the corresponding author upon reasonable request.

**Keywords:** Braiding Structure · Current Collector · Fiber · Lithium-Ion Battery

[1] a) M. Liao, L. Ye, Y. Zhang, T. Chen, H. Peng, *Adv. Electron. Mater.* **2019**, *5*, 1800456; b) H. Sun, X. Fu, S. Xie, Y. Jiang, H. Peng, *Adv. Mater.* **2016**, *28*, 2070; c) Y. H. Kwon, S.-W. Woo, H.-R. Jung, H. K. Yu, K. Kim, B. H. Oh, S. Ahn, S.-Y. Lee, S.-W. Song, J. Cho, H.-C. Shin, J. Y. Kim, *Adv. Mater.* **2012**, *24*, 5192; d) Y. Zhang, L. Wang, Z. Guo, Y. Xu, Y. Wang, H. Peng, *Angew. Chem. Int. Ed.* **2016**, *55*, 4487.

[2] a) Y. Zhang, Y. Zhao, J. Ren, W. Weng, H. Peng, *Adv. Mater.* **2016**, *28*, 4524; b) Y. Gao, H. Hu, J. Chang, Q. Huang, Q. Zhuang, P. Li, Z. Zheng, *Adv. Energy Mater.* **2021**, *11*, 2101809; c) J. He, C. Lu, H. Jiang, F. Han, X. Shi, J. Wu, L. Wang, T. Chen, J. Wang, Y. Zhang, H. Yang, G. Zhang, X. Sun, B. Wang, P. Chen, Y. Wang, Y. Xia, H. Peng, *Nature* **2021**, *597*, 57; d) M. Liao, C. Wang, Y. Hong, Y. Zhang, X. Cheng, H. Sun, X. Huang, L. Ye, J. Wu, X. Shi, X. Kang, X. Zhou, J. Wang, P. Li, X. Sun, P. Chen, B. Wang, Y. Wang, Y. Xia, Y. Cheng, H. Peng, *Nat. Nanotechnol.* **2022**, *17*, 372; e) L. Chen, J. Zhou, Y. Wang, Y. Xiong, J. Zhang, G. Qi, J. Cheng, B. Wang, *Adv. Energy Mater.* **2023**, *13*, 2202933.

[3] a) D. Wang, C. Han, F. Mo, Q. Yang, Y. Zhao, Q. Li, G. Liang, B. Dong, C. Zhi, *Energy Storage Mater.* **2020**, *28*, 264; b) S. Ling, X. Li, T. Zhou, R. Yuan, S. Sun, H. He, C. Zhang, *Adv. Mater.* **2023**, *35*, 2211201, ; c) J. Chang, Q. Huang, Y. Gao, Z. Zheng, *Adv. Mater.* **2021**, *33*, 2004419.

[4] a) A. Shodiev, M. Chouchane, M. Gaberscek, O. Arcelus, J. Xu, H. Oularbi, J. Yu, J. Li, M. Morcrette, A. A. Franco, *Energy Storage Mater.* **2022**, *47*, 462; b) J. Wu, X. Zhang, Z. Ju, L. Wang, Z. Hui, K. Mayilvahanan, K. J. Takeuchi, A. C. Marschilok, A. C. West, E. S. Takeuchi, G. Yu, *Adv. Mater.* **2021**, *33*, 2101275.

[5] a) Z. Guo, Y. Zhao, Y. Ding, X. Dong, L. Chen, J. Cao, C. Wang, Y. Xia, H. Peng, Y. Wang, *Chem* **2017**, *3*, 348; b) J. Ren, Y. Zhang, W. Bai, X. Chen, Z. Zhang, X. Fang, W. Weng, Y. Wang, H. Peng, *Angew. Chem. Int. Ed.* **2014**, *53*, 7864.

[6] a) Q. Chen, S. Sun, T. Zhai, M. Yang, X. Zhao, H. Xia, *Adv. Energy Mater.* **2018**, *8*, 1800054; b) J. Dang, R. Zhu, S. Zhang, L. Yang, X. Chen, H. Wang, X. Liu, *Small* **2022**, *18*, 2107869.

[7] a) Y. Wang, C. Chen, H. Xie, T. Gao, Y. Yao, G. Pastel, X. Han, Y. Li, J. Zhao, K. Fu, L. Hu, *Adv. Funct. Mater.* **2017**, *27*, 1703140; b) Z. Wu, K. Liu, C. Lv, S. Zhong, Q. Wang, T. Liu, X. Liu, Y. Yin, Y. Hu, D. Wei, Z. Liu, *Small* **2018**, *14*, 1800414.

[8] T. Hoshide, Y. Zheng, J. Hou, Z. Wang, Q. Li, Z. Zhao, R. Ma, T. Sasaki, F. Geng, *Nano Lett.* **2017**, *17*, 3543.

[9] F. Mo, G. Liang, Z. Huang, H. Li, D. Wang, C. Zhi, *Adv. Mater.* **2020**, *32*, 1902151.

[10] a) M. Chen, J. Ouyang, A. Jian, J. Liu, P. Li, Y. Hao, Y. Gong, J. Hu, J. Zhou, R. Wang, J. Wang, L. Hu, Y. Wang, J. Ouyang, J. Zhang, C. Hou, L. Wei, H. Zhou, D. Zhang, G. Tao, *Nat. Commun.* **2022**, *13*, 7097; b) K. Dong, X. Peng, J. An, A. C. Wang, J. Luo, B. Sun, J. Wang, Z. L. Wang, *Nat. Commun.* **2020**, *11*, 2868.

[11] M. Xu, B. Reichman, X. Wang, *Energy* **2019**, *186*, 115864.

[12] a) Y. Kuang, C. Chen, G. Pastel, Y. Li, J. Song, R. Mi, W. Kong, B. Liu, Y. Jiang, K. Yang, L. Hu, *Adv. Energy Mater.* **2018**, *8*, 1802398; b) J. Billaud, F. Bouville, T. Magrini, C. Villevieille, A. R. Studart, *Nat. Energy* **2016**, *1*, 16097.

[13] a) T. Wu, Z. Zhao, J. Zhang, C. Zhang, Y. Guo, Y. Cao, S. Pan, Y. Liu, P. Liu, Y. G, W. Liu, L. Dong, H. Lu, *Energy Storage Mater.* **2021**, *36*, 265; b) S. Lin, Y. Wang, Y. Chen, Z. Cai, J. Xiao, T. Muhmood, X. Hu, *Small* **2022**, *18*, 2104224.

[14] a) J. Zhao, H. Lu, Y. Zhang, S. Yu, O. I. Malyi, X. Zhao, L. Wang, H. Wang, J. Peng, X. Li, Y. Zhang, S. Chen, H. Pan, G. Xing, C. Lu, Y. Tang, X. Chen, *Sci. Adv.* **2021**, *7*, eabd6978; b) M. Chen, Y. Zhang, G. Xing, S. Chou, Y. Tang, *Energy Environ. Sci.* **2021**, *14*, 3323.

Manuscript received: March 11, 2023
Accepted manuscript online: April 11, 2023
Version of record online: May 3, 2023